

## Chapter 5

# Long-term cosmic ray modulation

### 5.1 Introduction

In this chapter, long-term cosmic ray modulation<sup>1</sup> in the heliosphere is discussed. As discussed in previous chapters, cosmic rays in the heliosphere are subjected to different modulation processes which include diffusion, convection, energy changes and drifts (see *Potgieter, 1998; Fichtner, 2005; Heber and Potgieter, 2006; Ferreira, 2009*, for an overview). As the activity of the Sun periodically changes from solar maximum to minimum conditions (every  $\sim 11$  years) we subsequently observe solar cycle related changes in cosmic ray intensities due to changes in the modulation environment. These observations have stimulated theoretical and modelling efforts (discussed below) in order to understand and appreciate the physics behind long-term cosmic ray modulation. This chapter discusses the drift/global interaction region (GMIR) based approach of *Le Roux and Potgieter (1995)* and the compound approach developed by *Ferreira (2002)* and *Ferreira and Potgieter (2004)* to describe the long-term time-dependent cosmic ray modulation in the heliosphere. At the end of this chapter, modelling results (using the compound approach) are shown in the inner (at Earth) and outer heliosphere (along the Voyager 1 and 2 trajectories) and are compared to different spacecraft observations. Insight into this approach is necessary to appreciate the improved new compound approach discussed in the next chapters.

### 5.2 CIRs, MIRs and GMIRs

As discussed in the previous chapters, the fast solar wind originates from coronal holes and the slow wind originates adjacent to or above the active regions (*Kunow and Lee, 1999*). These fast and slow solar wind streams interact with each other while propagating outwards and form interaction regions (*Burlaga and Ogilvie, 1970; Burlaga et al., 1985*). An interaction region (compression) is created where the fast wind runs into the slow wind ejected earlier while a rarefaction region is created where the slow wind lag behind the fast wind. Since the magnetic

---

<sup>1</sup>Note that in this work long-term modulation means modulation over a few solar cycles.

field is frozen into the solar wind plasma, it too is enhanced at the compression region of the solar wind. If this interaction regions are observed over two or more consecutive solar rotations, it is called a corotating interaction region (CIR) (*Burlaga, 1984; Rouillard et al., 2010*), since this interaction region is approximately stationary in a frame which corotates with the Sun. At  $\sim 1$  AU these CIRs generally produce no global effect on long-term modulation of the cosmic rays, apart from a transient decrease in intensities that is observed (*McDonald and Burlaga, 1997; Heber et al., 1999b; Burlaga et al., 2003a; Balogh et al., 2008*).

Beyond  $\sim 10$  AU these CIRs begin to spread and merge and interact to form merged interaction regions (MIRs) (*Le Roux, 1999*). MIRs are large regions of intense magnetic fields and this strong magnetic fields in turn modulates cosmic ray intensities. Both the Voyager spacecraft measure a decrease in cosmic ray intensities when a MIR (stronger magnetic field) passed a spacecraft and an increase in intensity is measured when a rarefaction region (weaker magnetic field) passed the spacecraft. From these spacecraft observations, *Burlaga et al. (1985)* found that long-term modulation of cosmic ray is related to the magnetic field  $B$ . These authors described cosmic ray intensity profile in the region between  $\sim 10$  AU and  $\sim 40$  AU using a simple first-order differential equation for the rate of change of cosmic ray intensities with the magnetic field profile observed at a spacecraft used as an input. This relation is called the "CR-B relation" (*Burlaga et al., 2001*) and is an empirical approach which contains no cosmic ray transport processes, and is given as,

$$\begin{aligned} \frac{d}{dt}(C_k) &= -D_k \frac{B(t)}{B} & \text{for } B(t) > B, \\ \frac{d}{dt}(C_k) &= R_k & \text{for } B(t) \leq B, \end{aligned}$$

where  $B$  is the magnitude of the Parker HMF,  $B(t)$  the magnitude of the measured HMF and  $C_k$  the cosmic ray counting rate. Also  $R_k$  and  $D_k$  are constants. From these equations it follows that if  $B(t)$  is stronger than  $B$ , cosmic ray intensity decreases proportional to  $\frac{B(t)}{B}$  and if  $B(t)$  is weaker than  $B$ , then an increase in cosmic ray intensity at a constant rate  $R_k$  is computed according to the "CR-B relation".

MIRs can be classified into three categories based on their geometry namely, corotating MIRs (CMIRs), Local MIRs (LMIRs) and global MIRs (GMIRs) (*McDonald and Burlaga, 1997*). CMIRs are formed when two or more CIRs merge and are of a spiral shape extending many AU in radial direction and are observed to fade beyond  $\sim 40$  AU from the Sun (*Le Roux, 1999*). CMIRs and rarefaction regions give rise to successive decreases and increases in cosmic ray intensities for a period of several months, but they produce no long-term cosmic ray modulation. LMIRs are formed from transient streams and have only a limited latitudinal and longitudinal extent. They do not extend around the Sun and they do not necessarily extend to high latitudes. LMIRs can cause temporary decreases in the cosmic ray intensities and have a significant effect on the cosmic rays in some localised volume in the outer heliosphere (*McDonald and Burlaga, 1997*).

MIRs merge beyond  $\sim 20$  AU to form GMIRs, which can become large in extent and capable of causing the large step-like decrease in cosmic ray intensities. GMIRs are quasi-spherical shells

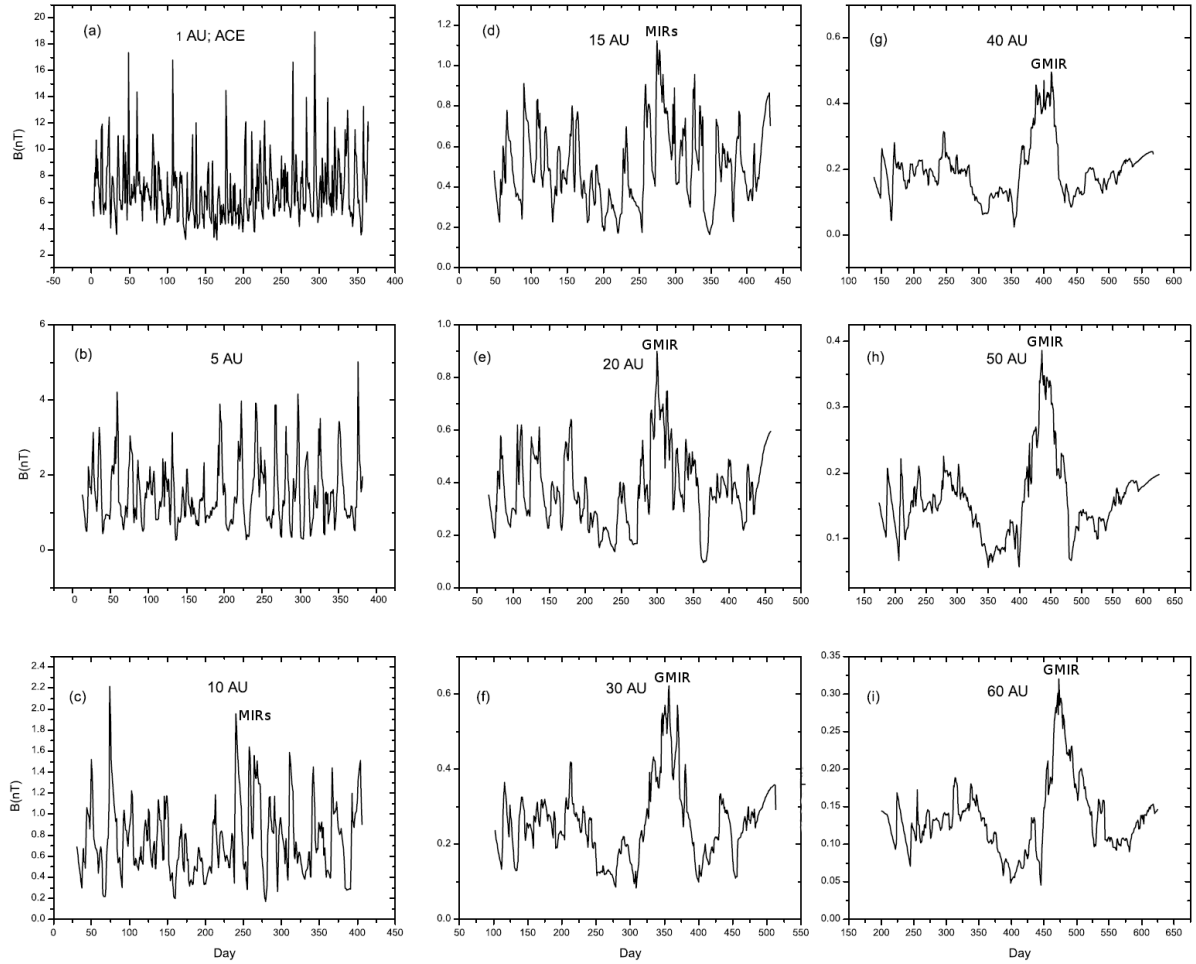


Figure 5.1: The computed radial evolution of the magnetic field strength profile from 1 AU to 60 AU illustrating how a GMIR is formed. Panel (a) shows ACE observations at 1 AU and panels (b)-(i) show the computed profiles of the magnetic field strength at 5, 10, 15, 20, 30, 40, 50 and 60 AU respectively. From *Burlaga et al. (2003b)*.

like MIRs extending  $360^\circ$  around the Sun and stretch at least  $30^\circ$  in heliolatitude and probably closing at the poles (*Potgieter, 1993; Le Roux, 1999; Le Roux and Fichtner, 1999a*).

The radial evolution of the magnetic field strength profile from 1 AU to 60 AU as computed by *Burlaga et al. (2003b)* is shown in Figure 5.1. This shows the forming of a GMIR. Panel (a) of the figure shows ACE observations at 1 AU and panels (b)-(i) show the computed magnetic field strength profile at 5, 10, 15, 20, 30, 40, 50 and 60 AU respectively using the ACE observations as input. From the figure it follows that a significant evolution in magnetic field strength profile occurs between 1 and 5 AU, although the evidence of a GMIR is not yet clear, which is consistent with observations (*Burlaga et al., 2003b*). A GMIR is beginning to form at 10 AU, between days 230 and 325 as shown in panel (c), representing relatively large enhancements in the magnetic field strength which is related to the growth of a series of MIRs. At 15 AU these MIRs are beginning to merge to form a GMIR with regions of strong magnetic fields. At 20 AU a GMIR can be seen evolving. From 30 AU to 60 AU the GMIR stands out clearly in the

computed magnetic field profile. The general form of the GMIR does not change significantly from 30-60 AU.

GMIRs have a life time of several solar rotations and move outward through the heliosphere at the solar wind speed (*Burlaga et al., 1985*), acting as a barrier to cosmic rays entering the heliosphere from all directions (*Potgieter and Le Roux, 1989*). The presence of a GMIR can be inferred from the cosmic ray observations which show a long-term step decreases in cosmic ray intensities over a large range of heliographic latitudes and longitudes (*McDonald and Burlaga, 1997*). Figure 5.2 shows 26-day averaged 130-225 MeV proton intensities along Pioneer 10 and IMP 8 spacecraft during the period 1977-1983. The 26-day averaged cosmic ray intensities which corresponds to  $\sim 1$  solar rotation, act as a filter that reduce the effects of short term cosmic ray modulation, e.g. less than 26 days. From the figure it follows that four step decreases in cosmic ray intensities are observed which is followed by a plateau. These are represented by roman numerals I, II, III and IV (*Fujii and McDonald, 1995*). These step-like cosmic ray intensity decreases are produced by GMIRs and they extend over a period of  $\sim 4$  to  $\sim 6$  months. During the period from solar minimum to maximum conditions  $\sim 4$ -5 of these step decreases in cosmic ray intensities usually takes place. These step decreases are prominent during moderate to high solar activity conditions when the changes in the HCS are no longer the main cause for the cosmic ray modulation, especially during  $A > 0$  polarity cycle when protons drift in along the poles (*McDonald and Burlaga, 1997; Potgieter, 1998; Ferreira, 2002*).

### 5.3 A brief history of long-term cosmic ray modulation models

Concerning the theoretical description of long-term cosmic ray modulation, it was shown by *Perko and Fisk (1983)* and *Le Roux and Potgieter (1989)* that in order to describe cosmic ray modulation over long periods, some form of propagating diffusion barriers are required. This is especially true for solar maximum activity periods when step decreases in cosmic ray intensities are observed. The largest of these diffusion barriers are global merged interaction regions (GMIRs) (*Burlaga et al., 1993*) as discussed above. Equally important to cosmic ray modulation are gradient, curvature and current sheet drifts (*Jokipii et al., 1977; Potgieter and Moraal, 1985*) as confirmed by the comprehensive modeling done by *Potgieter et al. (1993)* and *Le Roux and Potgieter (1995)*. These authors showed that it is possible to simulate, to a first-order, a complete 22-year modulation cycle by including a combination of drift effects and GMIRs in a time-dependent modulation model. The conclusion was made that drifts are mainly responsible for time-dependent modulation during moderate to minimum solar conditions with cosmic ray intensities changing mainly due to changes in the current sheet. However, towards solar maximum conditions GMIRs caused the intensities to decrease in a step-like manner with drifts becoming less dominant. For reviews see *Potgieter (1993)* and *Potgieter (1997)*.

However, *Cane et al. (1999)* and *Wibberenz et al. (2002)* argued that step-like decreases in cosmic ray intensities observed at Earth could not be primarily caused by GMIRs, because these de-

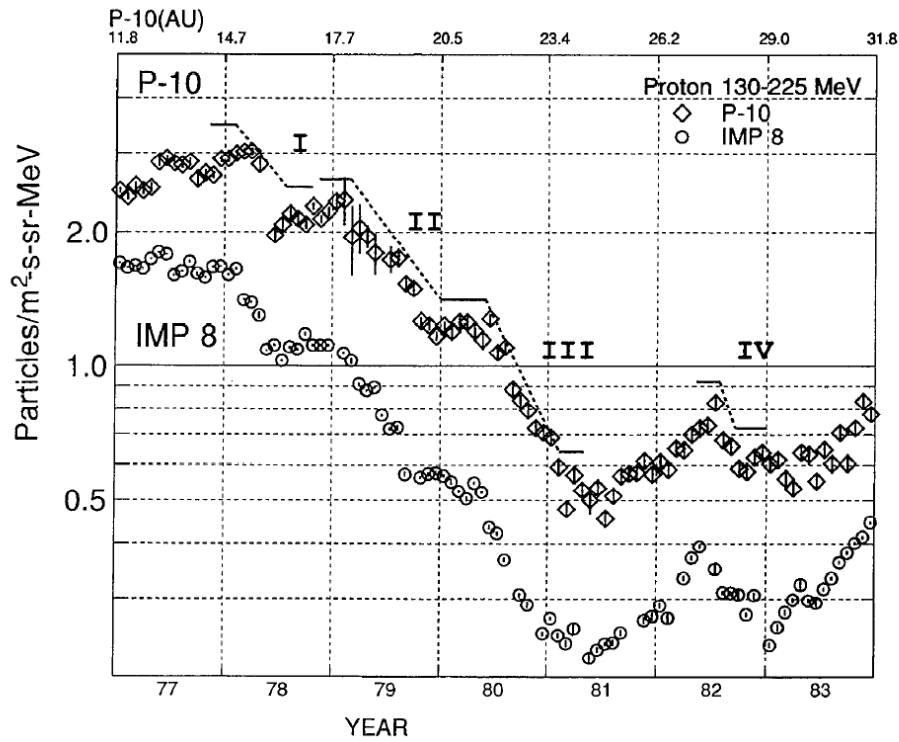


Figure 5.2: The 26 day averaged 130-225 MeV proton intensities from IMP 8 and Pioneer 10 during the period 1977 to the end of 1983. The Pioneer 10 heliocentric distances are indicated at the top axis of the plot. The four step decreases in cosmic ray intensities and the following plateau is represented by roman numerals I, II, III and IV. From *Fujii and McDonald (1995)*.

creases had occurred before any GMIRs could form beyond  $\sim 10$  AU (as shown in Figure 5.1). Instead, they suggested that time-dependent global changes in the HMF magnitude might be responsible for long-term modulation. This was tested by *Ferreira and Potgieter (2004)*, who showed that at neutron monitor energies, solar cycle related changes in the field magnitude, along with drifts, could explain these observations. For lower energies (i.e.  $\lesssim 5$  GeV) this is no longer the case and a combination of these approaches was suggested. This led *Ferreira and Potgieter (2004)* to introduce the compound approach, where all the transport (diffusion and drift) parameters are scaled with a time-dependent function based on the observed magnetic field at Earth and the current sheet tilt angle (*Hoeksema, 1992*). This resulted in diffusion coefficients and drifts changing over a solar cycle, with smaller values for solar maxima compared to solar minima.

As shown by *Ferreira and Potgieter (2004)*, *Ndiitwani et al. (2005)*, *Ferreira and Scherer (2006)*, *Manuel et al. (2011c)* and *Magidimisha (2011)* this approach incorporated in a numerical modulation model yields results in good agreement with spacecraft observations (Ulysses in particular) at various energies.

Next, these two approaches, in particular their implementation in numerical modulation models are discussed in more detail.

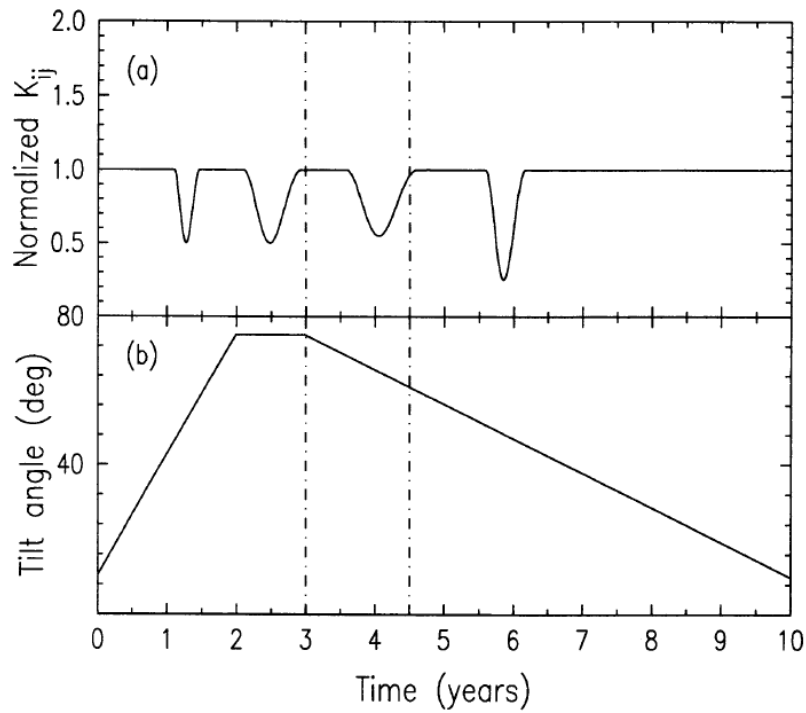


Figure 5.3: The top panel shows the assumed time-dependent normalised diffusion tensor at 10 AU in the equatorial plane. The four troughs are the effects of four GMIRs on the diffusion tensor during the 1977-1987 modulation cycle. The lower panel shows the assumed time-dependent tilt angle at 10 AU in the equatorial plane for the same period. The vertical dashed line shows the period of the HMF polarity reversal from an  $A > 0$  to an  $A < 0$  polarity cycle. From *Le Roux and Potgieter (1995)*.

## 5.4 Implementation of the GMIR/drift approach in a time-dependent modulation model

The long-term cosmic ray modulation in the heliosphere as simulated by *Potgieter et al. (1993)* and *Le Roux and Potgieter (1995)* using time-dependent 2D drift model with GMIRs incorporated is discussed in this section. A 2D time-dependent drift model with the waviness of the HCS as the only time-dependent parameter was used by *Potgieter and Le Roux (1992)* to describe cosmic ray modulation in the heliosphere. These authors found that drift is a dominant cosmic ray modulation process for tilt angles,  $\alpha \leq (35 \pm 5)^\circ$ . Later, *Le Roux and Potgieter (1995)* noticed that all aspects of the 22 year cosmic ray modulation cycle could not be reproduced with tilt angle as the only time-dependent parameter, especially the large step decrease in the cosmic ray intensities as shown in Figure 5.2. In order to model a complete 22 year cosmic ray modulation cycle, these authors indicated the importance of the propagating diffusion barriers, as proposed by *Perko and Fisk (1983)*, during moderate to high solar activity periods.

To incorporate propagating diffusion barriers (GMIRs) into the 2D time-dependent drift model *Le Roux and Potgieter (1995)* modelled regions of enhanced HMF (relative to the Parker field) that propagate radially outward with the solar wind speed. These authors described the diffusion tensor to be inversely proportional to the time-dependent HMF so that the GMIRs become

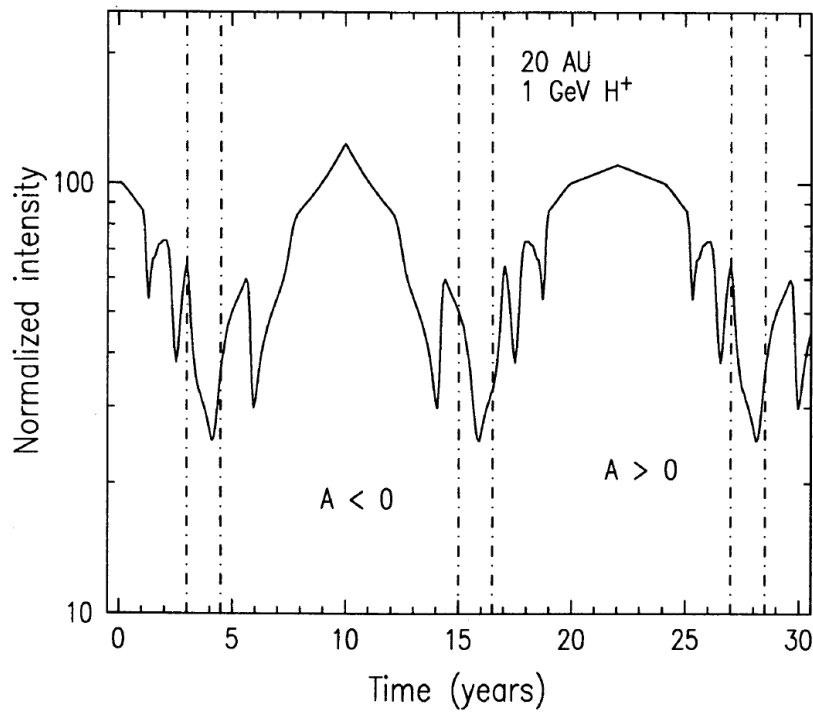


Figure 5.4: The simulated 22 year cosmic ray modulation cycle using a 2D time-dependent model with a combination of time-dependent drifts and GMIRs for a period of 30 years. The vertical dashed line shows the period of the HMF polarity reversal. From *Le Roux and Potgieter (1995)*.

partial barriers against the diffusing and drifting cosmic rays. Figure 5.3 top panel shows the assumed normalised diffusion tensor at 10 AU in the equatorial plane used by these authors. The four troughs seen in the top panel figure are the effects of the four GMIRs on the diffusion tensor during the 1977-1983 modulation cycle. The lower panel of the figure shows the assumed tilt angle at 10 AU in the equatorial plane as used in the model by these authors. The vertical dashed line shows the transition period where HMF polarity is reversed from an  $A > 0$  to an  $A < 0$  polarity cycle.

By combining drift and GMIRs in the model *Le Roux and Potgieter (1995)* successfully simulated a complete 11 and 22 year cosmic ray modulation cycle, as shown in Figure 5.4. The figure shows the model result for a period of 30 years using the time-dependent diffusion tensor and tilt angle as shown in Figure 5.3. The peak and plateau profile of the cosmic ray intensities during an  $A < 0$  and an  $A > 0$  polarity cycle, due to the proton drift along the HCS and along the poles, was successfully simulated along with the step decreases/increases as observed in long-term cosmic ray modulation profiles due to the passing of GMIRs .



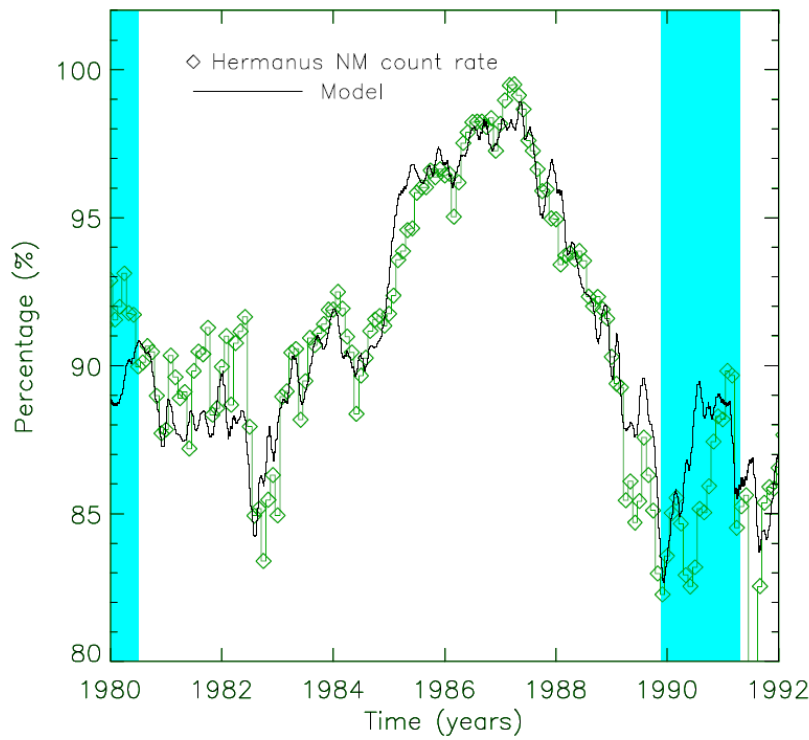


Figure 5.5: The 11 year normalised 16 GV cosmic ray modulation cycle as computed by the model compared to the Hermanus neutron monitor count rate expressed as percentage for the period 1980-1992,  $A < 0$  polarity cycle, with 100% in 1987. The shaded area shows the period of the HMF polarity reversal. From [Ferreira \(2002\)](#).

## 5.5 Implementation of the compound approach in a time-dependent modulation model

In this section, a brief description of the implementation of the compound approach of [Ferreira and Potgieter \(2004\)](#) in a numerical model is given. As suggested by [Cane et al. \(1999\)](#) and [Wibberenz et al. \(2002\)](#) (see Section 5.3), the time-dependent global changes in the HMF are more important for long-term modulation than GMIRs. This concept was tested by [Ferreira \(2002\)](#) and [Ferreira and Potgieter \(2004\)](#) by introducing time-dependence for the transport parameters. All diffusion and drift coefficients were multiplied by the following time-dependent function,

$$f(t) = \left( \frac{B_o}{B(t)} \right)^n, \quad (5.1)$$

where  $n$  is a constant and  $B_o = 5.0$  nT, the average magnitude of the measured HMF at Earth during solar minimum conditions (see Figure 2.16). The time-dependence in  $f(t)$  was introduced through  $B(t)$ , the time varying HMF measured at Earth. These time-dependent changes are then transported into the rest of the heliosphere with the solar wind,  $V = 400$  km.s<sup>-1</sup>. Using this function and a value of  $n = 1.0$  these authors successfully simulated a 11 year cosmic ray modulation cycle, as observed by neutron monitors on Earth.

Figure 5.5 shows the normalised 16 GV model result compared to the Hermanus neutron mon-



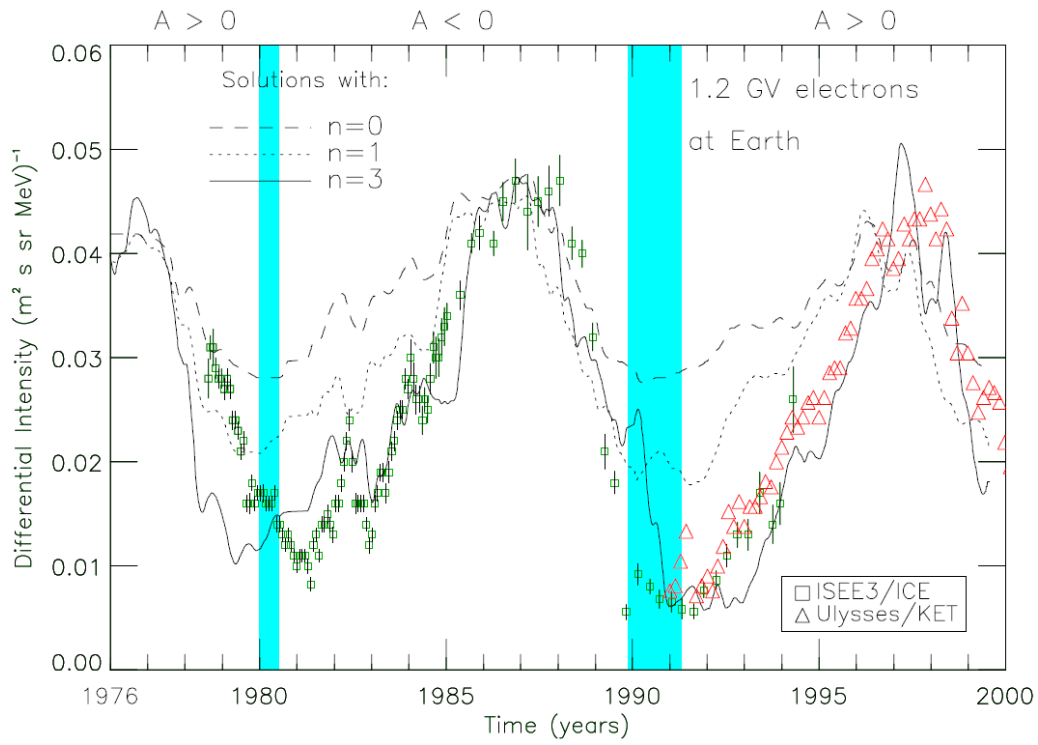


Figure 5.6: The computed intensities of 1.2 GV cosmic ray electrons at Earth for different  $n$  values (as given in Equation 5.1) during the period 1976-2000. The model results are compared to the ISSE/ICE and Ulysses/KET observations. The shaded area represents the time period when there is no well defined HMF polarity. Note that the unit of differential intensity is particles. $\text{m}^{-2}.\text{s}^{-1}.\text{sr}^{-1}.\text{MeV}^{-1}$ . From *Ferreira (2002)*.

itor count rate expressed as percentage for the period 1980-1992, an  $A < 0$  polarity cycle, with 100% in 1987. From the figure it follows that the model reproduced results (solid black line) which are compatible to neutron monitor observations (symbols). Also the model successfully reproduced the observed step-like decrease/increase in cosmic ray modulation profile without including GMIRs (*Ferreira, 2002; Ndiitwani, 2005; Magidimisha, 2011*).

However, this model failed to produce compatible model results for rigidities less than 5 GV when  $n = 1.0$  is assumed, suggesting a required improvement to the time-dependence used. Figure 5.6 shows the computed model result of 1.2 GV electrons at Earth for different  $n$  values as given in Equation 5.1, during the period 1976-2000 (from *Ferreira, 2002*). The model results are compared to the ISEE3/ICE and Ulysses/KET observations, shown as symbols. The shaded area represents the time period when there is no well defined HMF polarity. For  $n = 0.0$  (dashed line), the time-dependence as given by Equation 5.1 vanishes and the only time-dependent parameter in the model becomes the tilt angle,  $\alpha$ . For this  $n$  value the model transforms back to the model used by *Potgieter and Le Roux (1992)*. The computed results for  $n = 0$  are compatible with the observations only for solar minimum conditions (e.g.  $\sim 1985$ -1987 and  $\sim 1995$ -1997) but failed to produce a compatibility with observations during intermediate to solar maximum conditions. This confirms that the full 22 year cosmic ray modulation

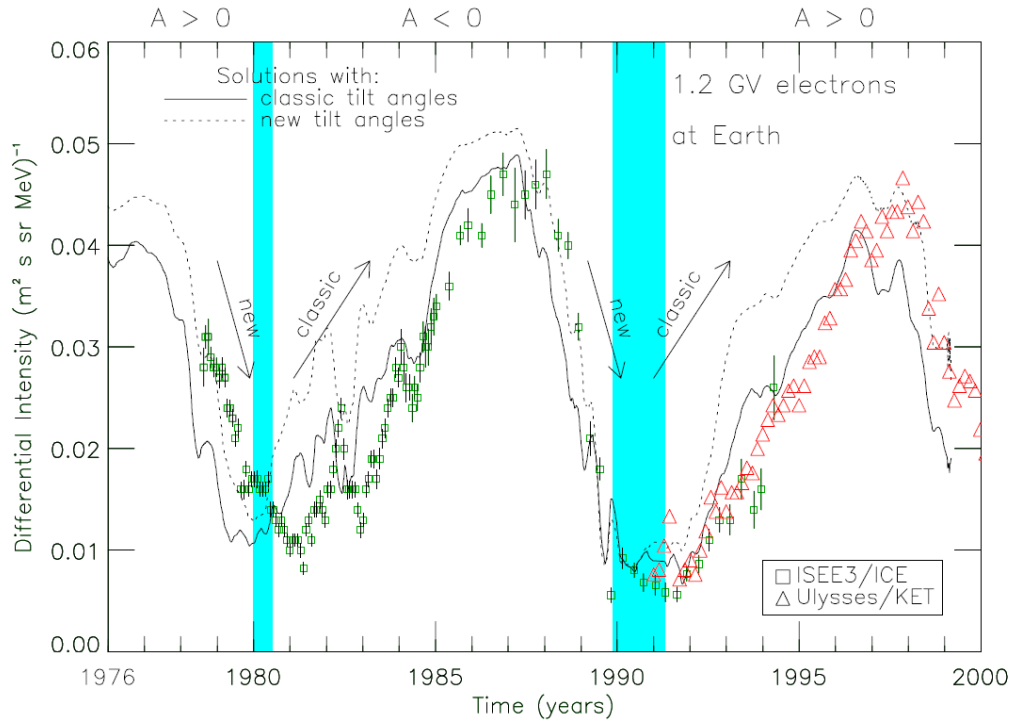


Figure 5.7: The computed results of 1.2 GV cosmic ray electrons at Earth using classic and new model tilt angles during the period 1976-2000. The model results are compared to the ISSE/ICE and Ulysses/KET observations. The shaded area represents the time period when there is no well defined HMF polarity. Note that the unit of differential intensity is particles.m<sup>-2</sup>.s<sup>-1</sup>.sr<sup>-1</sup>.MeV<sup>-1</sup>. From [Ferreira \(2002\)](#).

cycle could not be reproduced by only considering the HCS drift.

The dotted line representing  $n = 1.0$  shows that this modelling result is better compatible compared to the  $n = 0$  scenario for the solar minimum to intermediate conditions. However,  $n = 1.0$  failed to reproduce the observed amount of modulation, towards solar maximum. This  $n = 1.0$  scenario successfully reproduced 11 year neutron monitor modulation cycle (see Figure 5.5), but failed to compute a compatible result for rigidities less than 5 GV, i.e 1.2 GV electrons as shown in Figure 5.6. However, for  $n = 3.0$  (solid line) a more realistic result is computed but still not enough modulation is computed for the solar maximum period when compared to the observations. This suggests that a  $n > 3.0$  is required in Equation 5.1 for extreme solar maximum period and a  $n = 1.0$  for solar minimum conditions.

In order to model a  $n$  which varies between solar minimum to solar maximum [Ferreira \(2002\)](#) coupled it with the tilt angle, a parameter which depends on solar activity and which has a significant effect on the cosmic ray modulation. The time-dependence in  $n$  is given by,

$$n = \frac{\alpha(t)}{\alpha_o}, \quad (5.2)$$

where  $\alpha(t)$  is the measured time-dependent tilt angle and  $\alpha_o$  is a constant. So the time-

dependent function formulated by the compound approach can be given as,

$$f(t) = \left( \frac{B_o}{B(t)} \right)^{\left( \frac{\alpha(t)}{\alpha_o} \right)}. \quad (5.3)$$

Figure 5.7 shows computed 1.2 GV cosmic ray electron intensities using Equation 5.3 with  $\alpha_o = 11$  for two different tilt angle models (*Hoeksema, 1992*) namely, classic and new (see Chapter 2 and Figure 2.20). From the figure it follows that for the periods of increasing solar activity i.e. for the periods 1976-1980, 1987-1991 and 1997-2000, the new tilt angle (dotted line) model results are better compatible to the observations compared to the classic tilt angle (solid line) model results. However, for decreasing solar activity i.e. 1980-1987 and 1991-1997 periods, the classic model computed realistic model results when compared to the observations. For this study, a combination of new and classic tilt angle is used in accordance with the increasing and decreasing solar activity i.e. the tilt angle with the smallest rate of change in either an increasing or decreasing activity period is used in order to compute realistic results compatible with observations (see also *Ferreira and Potgieter, 2004; Ndiitwani, 2005; Manuel et al., 2011c*). The tilt angles used from here on is shown in Chapter 6, Figure 6.2.

## 5.6 Model calculations of cosmic ray intensities in the inner and outer heliosphere using the compound approach

In this section, the compound approach incorporated in a numerical model is used to calculate cosmic ray intensities in the inner and outer heliosphere. Because this approach forms the base of the improved/modified compound approach, the sensitivity of computations to different parameters used in this approach is first shown. The  $\alpha_o$  and  $B_o$  as given in Equation 5.3 are two free parameters, these parameters are varied to obtain compatible results compared to the observations. The time-dependence in the diffusion and drift coefficients, as given in Equation 5.3, is shown in Figure 5.8 for different  $\alpha_o$  values, namely 10, 20 and 40 respectively.

Figure 5.9 shows the 2.5 GV computed proton intensities along the Voyager 1 trajectory for different values of  $\alpha_o$  in Figure 5.8. The model results are compared to the  $> 70$  MeV Voyager 1 observations for compatibility. Note that after the shock crossing of Voyager 1 at 94 AU and in December 2004 (*Decker et al., 2005; Stone et al., 2005*), this channel may be contaminated by anomalous particles (*Stone et al., 2008*) so that the observations should be seen as an upper limit for galactic cosmic rays. The shaded region represents the transition periods for reversal of the HMF when there is no clear HMF polarity.

From the figure, it follows that a smaller  $\alpha_o$ , i.e. 10, computed much lower cosmic ray intensities along the Voyager 1 trajectory when compared to the observations, especially during the solar maximum periods. The  $\alpha_o = 20$  scenario computed improved compatibility when compared to the observations, but  $\alpha_o = 40$  computed results which are in general compatible with the Voyager observations. This  $\alpha_o$  is used from here on for the compound approach.

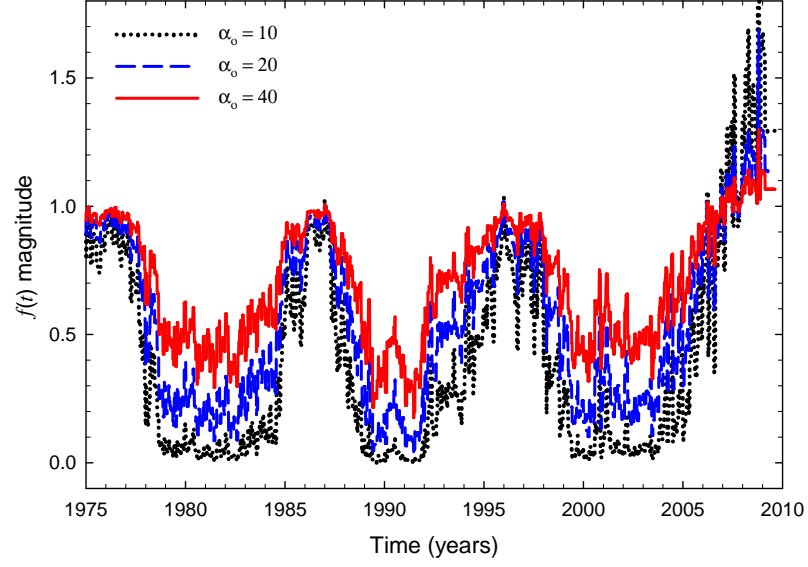


Figure 5.8: The function  $f(t)$  as given in Equation 5.3 for different  $\alpha_o$  values, 10 (dotted line), 20 (dashed line), 40 (solid line) respectively as used in the compound approach.

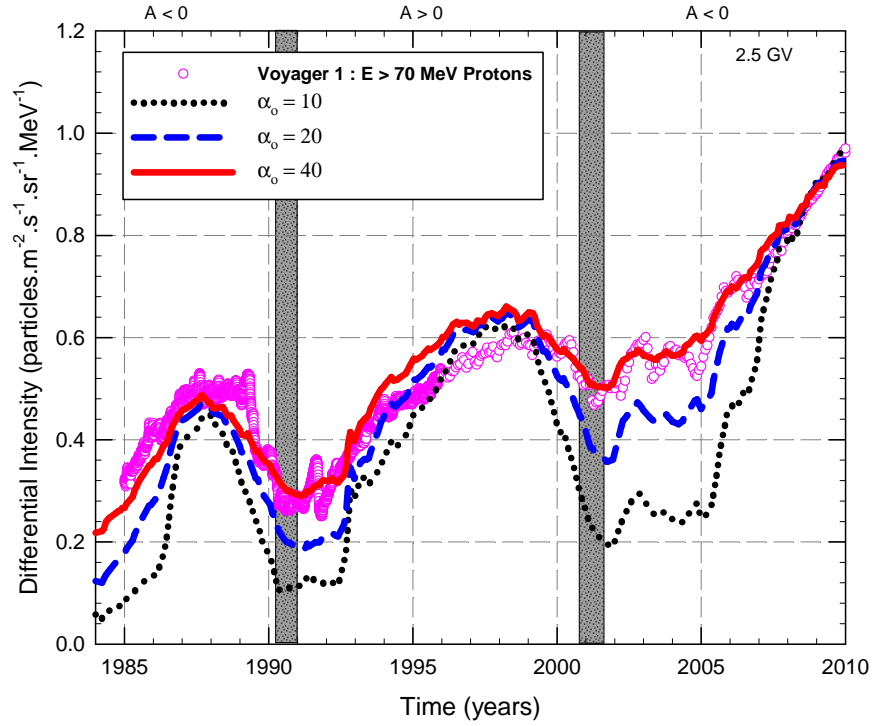


Figure 5.9: Computed 2.5 GV cosmic ray proton intensities along the Voyager 1 trajectory using the compound approach with  $\alpha_o$  values, 10 (dotted line), 20 (dashed line), 40 (solid line) respectively. The model results are compared to  $E > 70$  MeV proton observations (symbols) from Voyager 1 (data from <http://voyager.gsfc.nasa.gov>). The shaded region represents the transition periods for reversal of the HMF when there is no clear HMF polarity.

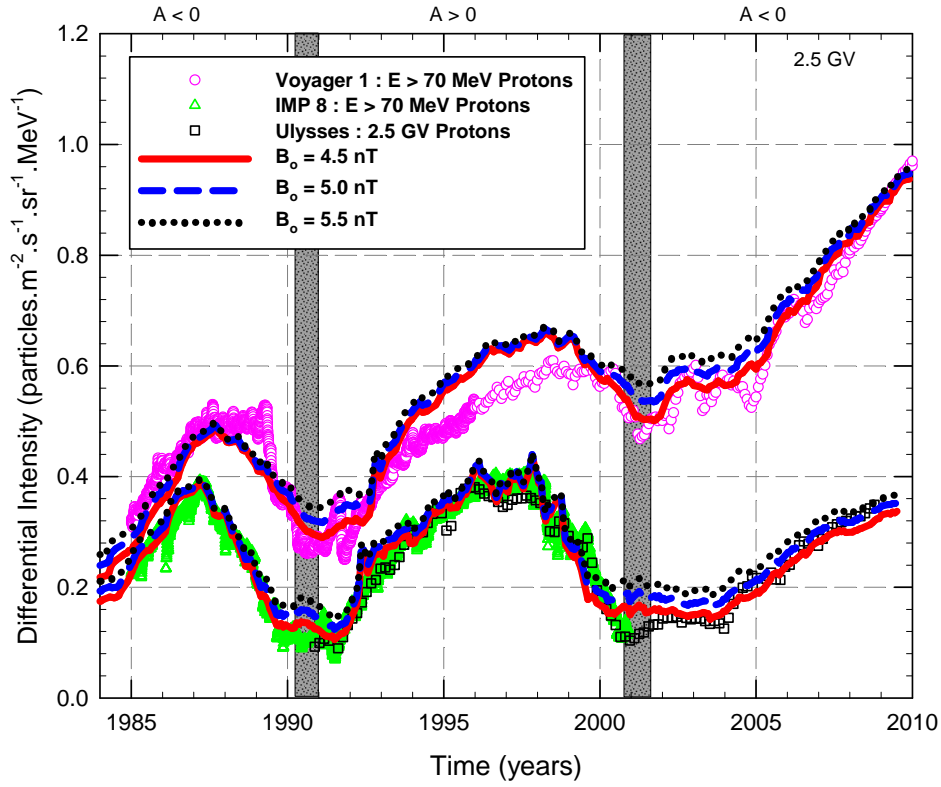


Figure 5.10: Computed 2.5 GV cosmic ray proton intensities at Earth and along the Voyager 1 trajectory are shown for  $B_o = 4.5$  nT (solid line),  $B_o = 5.0$  nT (dashed line) and  $B_o = 5.5$  nT (dotted line), respectively. The model Voyager 1 results are compared to  $E > 70$  MeV proton observations (circle symbols) from Voyager 1 (from <http://voyager.gsfc.nasa.gov>) and the model results at Earth are compared to  $E > 70$  MeV proton observations (triangle symbols) from IMP 8 (from <http://astro.nmsu.edu>) and  $\sim 2.5$  GV proton observations (square symbols) from Ulysses (*Heber et al., 2009*). The shaded region represents the transition periods for reversal of the HMF when there is no clear HMF polarity.

The effect of  $B_o$  (in Equation 5.3) on computed cosmic ray intensities using the compound approach is shown in Figure 5.10. The value of  $B_o$  is regarded as the average magnitude of the measured HMF at Earth during solar minimum conditions (see Figure 2.16). The model results are shown at Earth and along the Voyager 1 trajectory for three different values of  $B_o$ , namely, 4.5 nT (solid line), 5.0 nT (dashed line) and 5.5 nT (dotted line), respectively. The model results are then compared to the IMP 8 and Ulysses observations in the inner heliosphere and Voyager 1 observations in the outer heliosphere. From the figure it follows that there is no significant effect on the cosmic ray intensities during solar minimum conditions but during solar maximum periods the 4.5 nT results are more compatible compared to the observations in the inner and outer heliosphere. This smaller value of  $B_o$  leads to a larger amplitude in the transport coefficients between solar minimum and solar maximum. However, it can be concluded that the compound approach successfully reproduced the observations at Earth and along the Voyager 1 trajectory on a global scale.

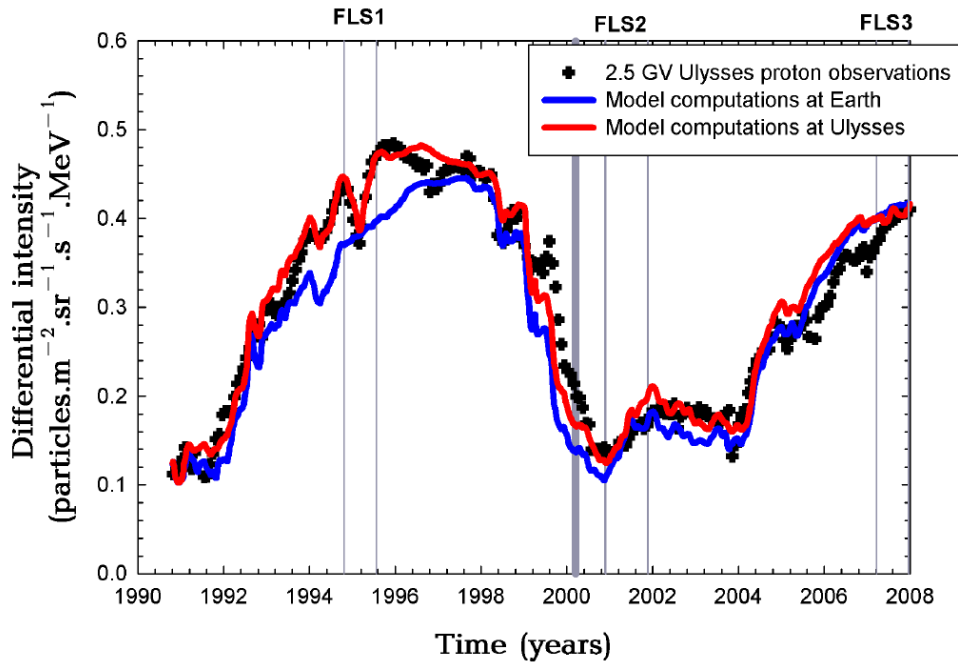


Figure 5.11: The computed results of 2.5 GV cosmic ray protons intensities at Earth (blue line) and along Ulysses trajectory (red line) from 1990 to 2008. The model results are compared to the  $\sim 2.5$  GV Ulysses observations. The thin vertical lines are the three fast latitude scan periods of the Ulysses spacecraft, occurring in  $\sim 1994.5$ - $1995.5$ ,  $\sim 2001$ - $2002$  and  $\sim 2007$ - $2008$  respectively. The thick vertical line at 2000.2 indicates the period where HMF polarity reversal takes place from  $A > 0$  to  $A < 0$ . From *Magidimisha (2011)*.

## 5.7 Cosmic ray latitudinal effects

As shown above, the compound approach computed realistic modulation when compared to cosmic ray intensity measurements from various spacecraft. This approach was tested by numerous authors namely, *Ferreira (2002)*, *Ferreira and Potgieter (2004)*, *Ndiitwani (2005)*, *Magidimisha (2011)* etc. A point to note is that the compound approach also successfully reproduced correct latitudinal gradients in cosmic ray intensities when compared to the observations along Ulysses and Voyager trajectories. This is shown in Figure 5.11 and 5.12.

Figure 5.11 shows the 2.5 GV proton differential intensities along the Ulysses trajectory (red line) and at Earth (blue line) from 1990 to 2008 as computed using the compound approach by *Magidimisha (2011)*. These model results are compared to the  $\sim 2.5$  GV Ulysses observations. The thin vertical lines in the figure are the three fast latitude scan (FLS) periods of the Ulysses spacecraft, occurred in  $\sim 1994.5$ - $1995.5$ ,  $\sim 2001$ - $2002$  and  $\sim 2007$ - $2008$  respectively. The thick vertical line at 2000.2 indicates the period where HMF polarity reversal took place from  $A > 0$  to  $A < 0$ . From the figure it follows that the compound approach successfully reproduced  $\sim 2.5$  GV proton observations along the Ulysses trajectory. During the  $A > 0$  polarity cycle, protons drift in along the polar regions and exit outward through the HCS. Therefore, a higher cosmic ray intensity is expected at polar regions when compared to the equatorial plane. This

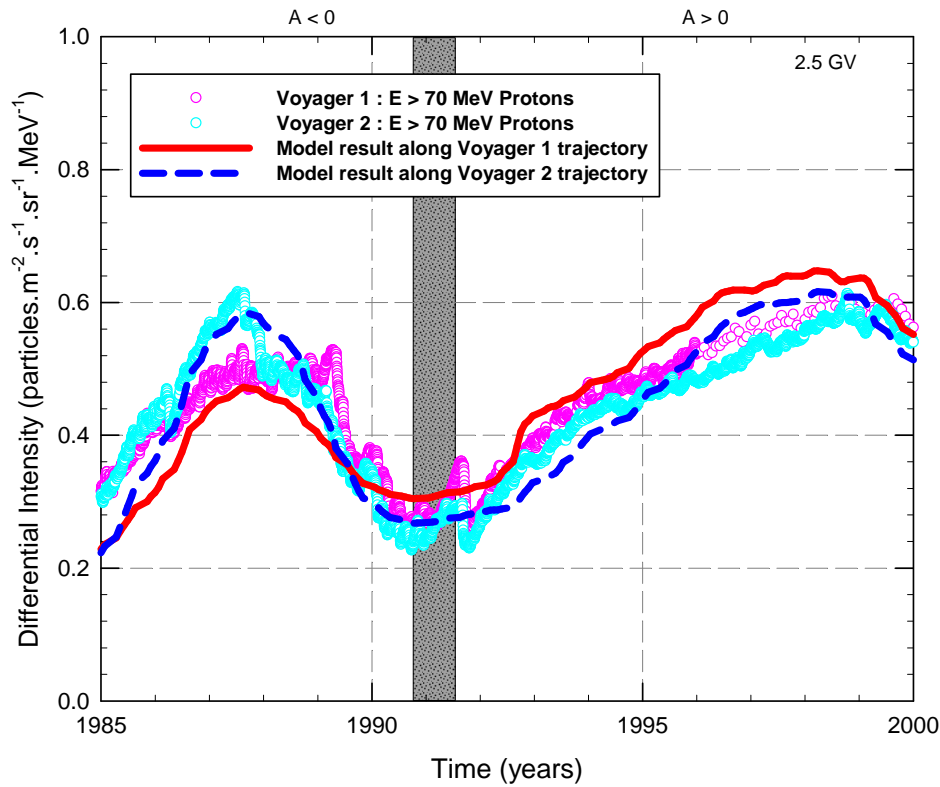


Figure 5.12: Computed 2.5 GV cosmic ray proton intensities along the Voyager 1 and 2 trajectories compared to  $E > 70$  MeV proton observations from Voyager 1 (pink circled symbols) and Voyager 2 (cyan circled symbols). The shaded region represents the transition periods for reversal of the HMF when there is no clear HMF polarity. The Voyager 1 and 2 data from <http://voyager.gsfc.nasa.gov>.

latitudinal gradient in cosmic ray intensities is evident when comparing the model results at Earth with those along the Ulysses trajectory during an  $A > 0$  polarity cycle. These two computed results deviate significant when Ulysses moved towards high heliolatitudes.

The Ulysses first fast latitude scan (FLS1) took place during a solar minimum with  $A > 0$  polarity cycle and this FLS1 period shows the latitudinal effect much clearly. However, during the second fast latitude scan (FLS2), which took place at a solar maximum period, no clear latitudinal dependence is found. Also, the third fast latitude scan (FLS3) which took place during a solar minimum with an  $A < 0$  polarity cycle, no clear latitudinal gradient is found for protons drifting along the HCS. *Magidimisha* (2011) also shown that for electrons the opposite happens; no clear latitudinal dependence was thus found for FLS1 and FLS2, but for FLS3 a significant dependence is computed.

Another example of latitudinal gradients is shown in Figure 5.12 for the period 1985-2000. The figure shows the computed 2.5 GV cosmic ray proton intensities along the Voyager 1 and Voyager 2 trajectories compared to the  $E > 70$  MeV proton observations from Voyager 1 and 2. The Voyager 1 and 2 trajectories are shown in Figure 2.29. The shaded region in Figure



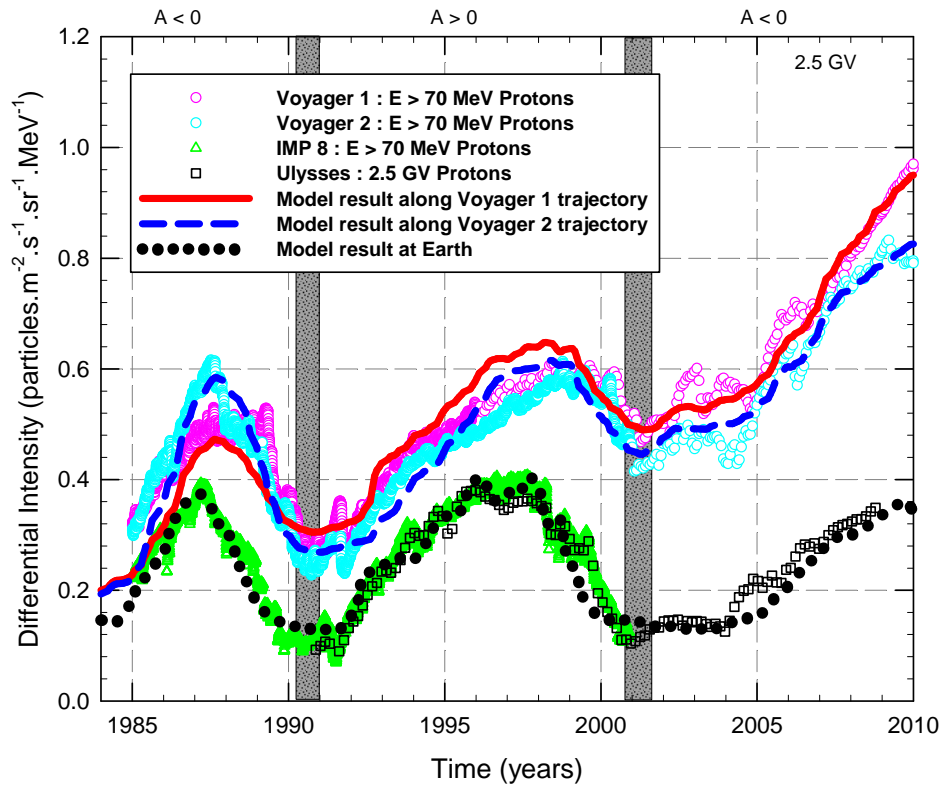


Figure 5.13: Computed 2.5 GV cosmic ray proton intensities at Earth and along the Voyager 1 trajectory. The model Voyager 1 and Voyager 2 results are compared to  $E > 70$  MeV proton observations from Voyager 1 (pink circles) and Voyager 2 (cyan circles). The model results at Earth are compared to  $E > 70$  MeV proton observations (triangle symbols) from IMP 8 (from <http://astro.nmsu.edu>) and  $\sim 2.5$  GV proton observations (square symbols) from Ulysses (Heber *et al.*, 2009). The shaded region represents the transition periods for reversal of the HMF when there is no clear HMF polarity. The Voyager 1 and 2 data from <http://voyager.gsfc.nasa.gov>.

5.12 represents the transition periods for reversal of the HMF when there was no clear HMF polarity. During the period  $\sim 1987$ -1989 Voyager 1 went to higher heliolatitudes while Voyager 2 stayed close to the equatorial plane. The cosmic ray observations for this period show a latitudinal dependence in cosmic ray intensities, Voyager 1 located at higher heliolatitudes measuring lower cosmic ray intensities compared to Voyager 2. This is due to the proton drift along the HCS during the  $A < 0$  polarity cycle and a higher cosmic ray intensity is observed in the equatorial regions where Voyager 2 was located for this period. From the figure it follows that the model successfully reproduced the observed latitudinal dependence when using the compound approach. However, during an  $A > 0$  polarity cycle protons drift in through the polar regions and are insensitive to the conditions in the equatorial regions. The observed small difference in cosmic ray intensities between the Voyager 1 and Voyager 2 during this period is due to the radial gradients in cosmic ray intensities due to the distance of these two spacecraft from the Sun as shown in Figure 2.29. See also Le Roux and Potgieter (1992); Potgieter and Le Roux (1992, 1994).

An optimal model result using the compound approach at Earth and along both Voyager trajectories are shown in Figure 5.13. The figure shows that the compound approach computed compatible 2.5 GV cosmic ray proton intensities in the inner and outer heliosphere when compared to different spacecraft observations.

It is important to note that the compound model is based on an empirical approach where model results were compared to observations to construct a realistic time-dependence in the transport coefficients due to a lack of clear theory on time-dependence of diffusion and drift coefficients. In the next chapter, this compound approach is modified into a new compound approach where the time-dependence of the different transport coefficients are incorporated using the newest theory. In this improved approach, solar cycle related changes in the transport coefficients are due to changes in basic turbulence quantities like magnetic field magnitude and variance.

## 5.8 Summary

In this chapter, time-dependent cosmic ray modulation was discussed. The GMIR/drift and compound approach to model cosmic ray intensities over a solar cycle were discussed. The GMIR/drift approach developed by *Le Roux and Potgieter (1995)* combined drift effects and GMIRs (propagating diffusion barriers) to compute time-dependent cosmic ray modulation in the heliosphere. These authors successfully simulated an 11 and a 22 year cosmic ray modulation cycle by incorporating GMIRs into the 2D time-dependent drift model as regions of enhanced HMF that propagate radially outwards with solar wind speed. Both peak and plateau profiles observed in the cosmic ray intensities during different polarity cycles and the step decreases/increases as observed towards solar maxima was successfully computed.

Later, *Ferreira (2002)* and *Ferreira and Potgieter (2004)* developed the compound approach considering the time-dependent global changes in the HMF and tilt angle to construct a time-dependence for all transport coefficients. Such a dependence was constructed by comparing the model results with different observations during consecutive solar cycles. As shown, this approach successfully computed compatible cosmic ray intensities in the inner and outer heliosphere when compared to observations (*Ferreira, 2002; Ndiitwani, 2005*). The compound approach also successfully reproduced correct latitudinal gradients in the cosmic ray intensities when compared to observations along Ulysses and Voyager trajectories (*Ndiitwani, 2005*). However, recent developments in the theoretical work on the transport parameters (*Teufel and Schlickeiser, 2002, 2003; Shalchi et al., 2004; Minnie et al., 2007; Engelbrecht, 2008*) warrant the compound approach to be revisited. Such a modified compound approach, where solar cycle related changes in the transport coefficients are related to changes in basic turbulence quantities, will be discussed in next chapter.